

Geometry-dependent two-photon absorption followed by free-carrier absorption in AlGaAs waveguides

DANIEL H. G. ESPINOSA,^{1,†} STEPHEN R. HARRIGAN,^{2,†} KASHIF M. AWAN,³ PAYMAN RASEKH,¹ AND KSENIA DOLGALEVA^{1,2,*}

¹*School of Electrical Engineering and Computer Science, University of Ottawa, Ottawa, Ontario K1N 6N5, Canada*

²*Department of Physics, University of Ottawa, Ottawa, Ontario K1N 6N5, Canada*

³*Stewart Blusson Quantum Matter Institute, Vancouver, BC V6T 1Z4, Canada*

[†]*These authors contributed equally to this work.*

*ksenia.dolgaleva@uottawa.ca

Abstract: Nonlinear absorption can limit the efficiency of nonlinear optical devices. However, it can also be exploited for optical limiting or switching applications. Thus, characterization of nonlinear absorption in photonic devices is imperative. This work used the nonlinear transmittance technique to measure the two-photon absorption coefficients (α_2) of AlGaAs waveguides in the strip-loaded, nanowire, and half-core geometries in the wavelength range from 1480 to 1560 nm. The highest α_2 values of 2.4, 2.3, and 1.1 cm/GW were measured at 1480 nm for a 0.8-nm-wide half-core, 0.6-nm-wide nanowire, and 0.9-nm-wide strip-loaded waveguides, respectively, with α_2 decreasing with increasing wavelength. The free-carrier absorption cross-section was also estimated from the nonlinear transmittance data to be around 2.2×10^{-16} cm² for all three geometries. Our results contribute to a better understanding of the nonlinear absorption in heterostructure waveguides of different cross-sectional geometries. We discuss how the electric field distribution in the different layers of a heterostructure can lead to geometry-dependent effective two-photon absorption coefficients. More specifically, we pinpoint the third-order nonlinear confinement factor as a design parameter to estimate the strength of the effective nonlinear absorption, in addition to tailoring the bandgap energy by varying material composition.

© 2021 Optical Society of America

1. Introduction

Aluminum gallium arsenide (AlGaAs) is an established material platform among III-V semiconductors considered for nonlinear photonics applications. The nonlinear optical properties of waveguides made of AlGaAs heterostructures on GaAs substrates, and more recently on SiO₂ and sapphire substrates, have been exploited to demonstrate efficient four-wave mixing [1–3], orthogonal four-wave mixing [4], wavelength conversion [5, 6], frequency comb generation [7], sum- and difference-frequency generation [8] and second-harmonic generation [9, 10]. Additionally, the near perfect lattice matching between GaAs and AlAs allows arbitrary tuning the aluminium fraction x in an Al _{x} Ga_{1- x} As alloy. By tailoring the aluminium fraction, which impacts material properties such as the bandgap energy, devices can be fabricated with tunable linear and nonlinear absorption and refraction, and dispersion [3, 11–14].

One factor limiting the efficiency of nonlinear optical interactions are nonlinear losses associated with the nonlinear optical material. For this reason, it is important to perform a thorough nonlinear optical characterization of new materials and devices to understand their practical limit. Nonlinear absorption (NLA) can also be applied in optical limiting [15] or all-optical switching devices based on free-carrier dispersion, where the free-carriers are generated by two-photon absorption (2PA) [16, 17]. Investigating the influence of waveguide geometry on the effective two-photon

absorption coefficient is crucial for predicting and designing useful devices.

We have recently reported on the experimental study of four-wave mixing (FWM) in AlGaAs waveguides of three different geometries: strip-loaded, nanowire, and half-core [see Fig. 1 (c)–(e), showing the cross-section of each geometry] [1]. In the strip-loaded waveguide, the light propagates in the slab region below the ridge defined in the upper cladding, whereas in the nanowire, the guiding layer is etched through. The nanowire allows the realization of narrower waveguides for stronger light confinement, while the strip-loaded waveguide exhibits the lowest propagation loss. The half-core waveguide geometry represents a compromise between the other two, featuring stronger light confinement than the strip-loaded design but lower propagation loss than the nanowire design. Comparative analysis of FWM indicated that the NLA of a pump beam with a pulse width of 3 ps impacts the FWM efficiency of each geometry differently, mainly for wavelengths longer than 1500 nm. This result motivated further investigations to better understand NLA processes in these geometries [1].

Nonlinear absorption in AlGaAs strip-loaded waveguides with $\text{Al}_{0.18}\text{Ga}_{0.82}\text{As}$ as the guiding layer composition has been studied for waveguide widths ranging from 5 to 6 μm [18–20]. The 2PA coefficient in a 1.5- μm -wide nanowire with $\text{Al}_{0.13}\text{Ga}_{0.87}\text{As}$ as the guiding layer composition has also been measured [21]. However, there are no reports on the influence of the nonlinear absorption on the nonlinear optical performance of AlGaAs nanowires with the guiding layer composition $\text{Al}_{0.18}\text{Ga}_{0.82}\text{As}$, and no reports on measuring 2PA in half-core waveguides, representing a recently proposed geometry [1, 22]. Moreover, systematic comparison of 2PA in waveguides of different geometries having the same guiding layer composition has not been performed.

Advances in nanofabrication, such as electron-beam lithography and plasma etching, made possible the realization of devices as narrow as hundreds of nanometers in width [3]. To facilitate coupling light into such devices, it is typical to use wider coupling waveguides and to taper them down to the width of the narrower part, as indicated in Fig. 1 (a). Using tapers, however, complicates the analysis of the nonlinear optical performance of such devices. The coupling part itself may present nonlinear effects, making the evaluation of the irradiance in the narrower parts more challenging. Furthermore, the NLA measurements in AlGaAs waveguides did not consider free-carrier absorption (FCA), but some works in GaAs/AlGaAs waveguides and GaAs/AlGaAs multiple-quantum-well waveguides report the presence of 2PA followed by FCA as the NLA mechanism [23–25]. Proper separation of these effects is crucial for a proper extraction of the 2PA coefficient from the NLA data.

In this work, we measure the 2PA coefficient in the wavelength range of 1480 nm to 1560 nm, falling in the optical communications C-band, of AlGaAs waveguides of strip-loaded, nanowire, and half-core geometries, which all have $\text{Al}_{0.18}\text{Ga}_{0.82}\text{As}$ as the guiding layer composition. This work represents the first comparative study of the influence of the NLA on various waveguide geometries under identical experimental conditions, and the first NLA measurement performed in a half-core waveguide. The data analysis includes the effect of FCA with an estimation of the FCA cross-section. Our method also addresses the effect of nonlinear absorption in the coupling parts of the waveguides to properly deduce the 2PA coefficient of the narrowest parts of the waveguides, which be of interest for future measurements of 2PA in tapered devices. Finally, we discuss how the intensity distribution in the different layers of the waveguides influences the results.

The rest manuscript is organized as follows. Section 2 presents the waveguides geometries, composition, simulations of the intensity distributions, experimental methods, and the models of nonlinear absorption used in this work. Section 3 reports the 2PA coefficient and FCA cross-section results for each geometry, as a function of the wavelength. Section 4 discusses the effective 2PA coefficient dependence on the nonlinear confinement factor, which is geometry-dependent.

2. Experimental

2.1. AlGaAs waveguides

The waveguides of the nanowire, strip-loaded, and half-core geometries were fabricated using e-beam lithography followed by RIE/ICP dry etching. A 2- μm -wide coupling region was used to couple the light to and from the < 1- μm -wide (“nanosectional”) part [see Fig. 1 (a)]. To study the effect of the 2- μm -wide coupling region, we made straight 2- μm -wide waveguides [Fig. 1 (b)], called reference waveguides. The cross-sectional dimensions, intensity distribution and aluminum fraction are presented in Fig. 1 (c) to (h). The intensity distribution and the effective mode area (A_{eff}) were calculated using the finite difference eigenmode (FDE) solver of *Lumerical Mode Solutions*. The FDE solver calculates the effective mode area using the equation

$$A_{\text{eff}} = \frac{\left[\int_{-\infty}^{\infty} \int_{-\infty}^{\infty} |E(x, y)|^2 dx dy \right]^2}{\int_{-\infty}^{\infty} \int_{-\infty}^{\infty} |E(x, y)|^4 dx dy}. \quad (1)$$

Other details of the waveguides design optimization, fabrication, and characterization are presented in references [1, 26].

2.2. Experimental setup

A schematic of the experimental setup is shown in Fig. 2. We used a Ti:Sapphire laser and optical parametric oscillator (OPO), with the temporal full width at half-maximum of $\tau_{\text{FWHM}} = 3$ ps and the repetition rate of $f_p = 76.6$ MHz. While the OPO wavelength can range from 1000 nm to about 3700 nm, we selected the wavelengths from $\lambda = 1480$ nm to $\lambda = 1560$ nm to work in the same range where FWM was observed in our devices [1]. The rotation of a half-wave plate controls the beam power while a polarizing beam splitter keeps the polarization constant. We used objective lenses in the coupling stage to couple the light to and collect the light from the waveguides. The average power at the waveguide output (P_{out}) is measured as a function of the average power at the waveguide input (P_{in}) by the use of photodetectors and a power meter.

2.3. Linear propagation loss measurement

The linear loss coefficient α_1 and the Fresnel coefficient [$R = 0.30(1)$] were measured in the reference waveguides by the Fabry-Perot method, using a tunable CW laser beam (model TSL-710, Santec inc.) [1, 3, 27]. The linear loss coefficients of the nanosectional parts were measured using the linear region of the plot P_{out} vs. P_{in} . The coupling efficiencies (η_C) were determined as 0.27(1), 0.11(1) and 0.20(3) for the strip-loaded, nanowire and half-core geometries, respectively. As the main focus of this work is the nonlinear loss, the linear loss coefficient (α_1) values and the related discussions are presented in Appendix A. More details on the method of the linear loss measurements are also given in ref. [1].

2.4. Nonlinear loss

For the nonlinear absorption analysis, the change in the light irradiance $I(z)$ with the propagation distance in the waveguide z needs to be quantified, and this is done by solving the differential equation

$$\frac{dI}{dz} = -\alpha_1 I - \alpha_2 I^2 - \alpha_x I^3, \quad (2)$$

where the parameter α_2 is the 2PA coefficient, and the parameter α_x can either be associated with the three-photon absorption (3PA) or FCA, as we will detail below.

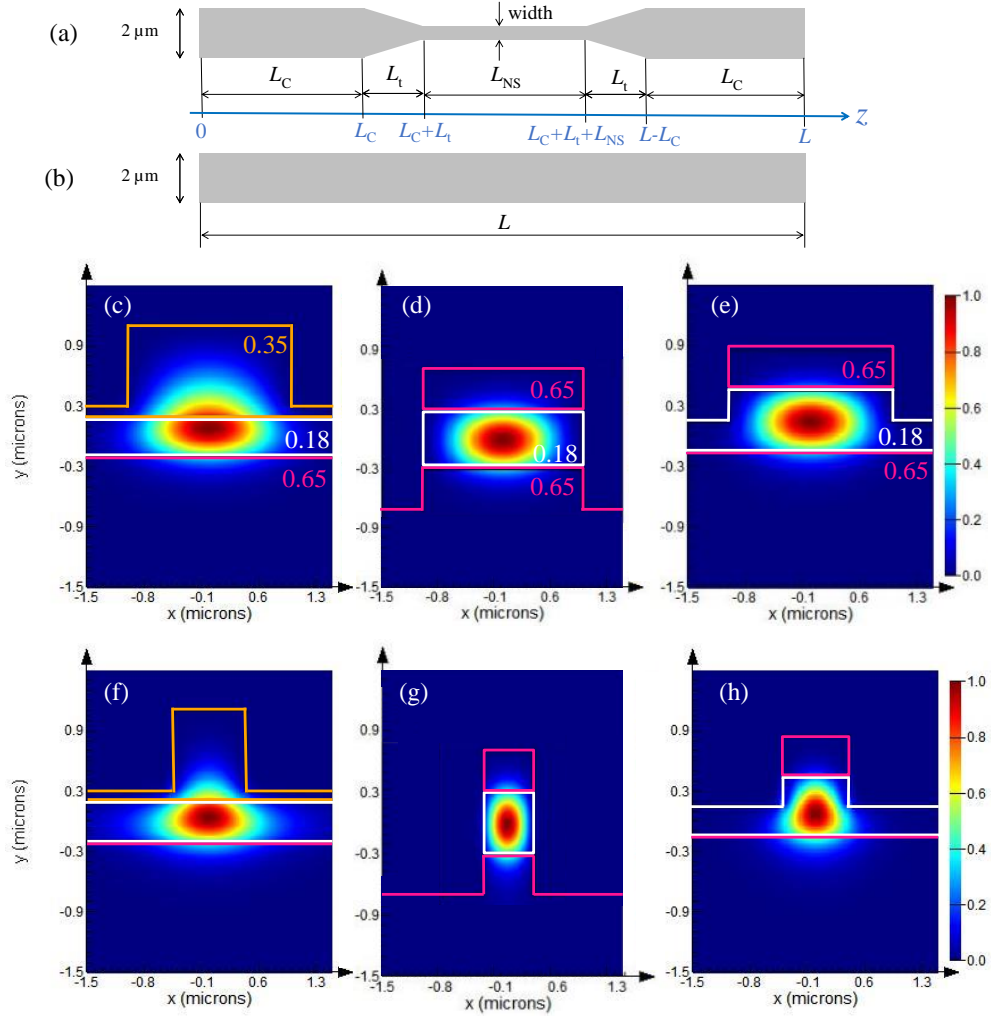


Fig. 1. (color on-line) Top-down view of the tapered (a) and reference (b) waveguides. In this work, we call the narrower part of the tapered device “nanosectional part.” (c)-(h) Waveguide cross-sections with the optical intensity distributions of the fundamental transverse-electric (TE) mode at 1500 nm in $2\text{-}\mu\text{m}$ -wide strip-loaded (c), nanowire (d) and half-core (e) coupling waveguides, and $0.9\text{-}\mu\text{m}$ -wide strip-loaded (f), $0.6\text{-}\mu\text{m}$ -wide nanowire (g), and $0.8\text{-}\mu\text{m}$ -wide half-core (h) nanosectional parts. The numbers on the images represent the aluminum fraction x of each layer. $L = 5.26 \text{ mm}$ and $L_{NS} = 1 \text{ mm}$ for the strip-loaded, $L = 5.33 \text{ mm}$ and $L_{NS} = 2 \text{ mm}$ for the nanowire, and $L = 5.87 \text{ mm}$ and $L_{NS} = 1 \text{ mm}$ for the half-core waveguides. For all waveguide geometries, $L_t = 0.2 \text{ mm}$ and $L_C = (L - L_{NS} - 2L_t)/2$.

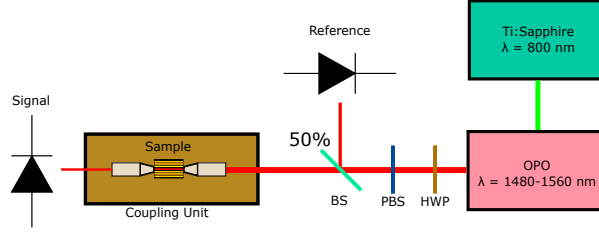


Fig. 2. (color on-line) Diagram of the experimental setup used to perform the nonlinear transmittance technique. OPO - optical parametric oscillator, HWP - half-wave plate, PBS - polarizing beam splitter, BS - beam splitter.

For the reference devices, the irradiance coupled into the waveguide, at its beginning $[I(0)]$ and end $[I(L)]$, is calculated by dividing the peak power by the effective mode area, according to

$$I(0) = \frac{0.94(1-R)\eta_C P_{in}}{\tau_{FWHM} f_p A_{eff}} \quad (3)$$

and

$$I(L) = \frac{0.94 P_{out}}{(1-R)\tau_{FWHM} f_p A_{eff}}, \quad (4)$$

respectively, where η_C is the coupling efficiency and the factor 0.94 comes from the assumption of a Gaussian temporal profile.

When the nonlinear absorption is dominated by the 2PA mechanism, ($\alpha_x = 0$) the solution of Eq. (2) is given by

$$I(z) = \frac{I(0)\exp(-\alpha_1 z)}{1 + \alpha_2 I(0) L_{eff}}, \quad (5)$$

with $L_{eff} = [1 - \exp(-\alpha_1 z)]/\alpha_1$. Conversely, if 2PA is negligible ($\alpha_2 = 0$) and the dominant mechanism is 3PA, α_x is the 3PA coefficient ($\alpha_x = \alpha_3$), and solution of Eq. (2) is given by

$$I(z) = \frac{I(0)\exp(-\alpha_1 z)}{\sqrt{1 + 2\alpha_3 I^2(0) L'_{eff}}}, \quad (6)$$

where $L'_{eff} = [1 - \exp(-2\alpha_1 z)]/(2\alpha_1)$.

For the case where both α_2 and α_x are non-vanishing, Eq. (2) is usually solved numerically. One useful approximate solution is of the form [28]

$$I(z) = \frac{I(0)\exp(-\alpha_1 z)}{1 + \left(\alpha_2 - \frac{\alpha_1 \alpha_x}{\alpha_2}\right) I(0) L_{eff} + \frac{\alpha_x [\alpha_1 + \alpha_2 I(0)]}{\alpha_2^2} \log [1 + \alpha_2 I(0) L_{eff}]}. \quad (7)$$

Eq. (7) can be applied to the cases where both 2PA and 3PA are present. For semiconductors, the simultaneous absorption of three photons would promote an electron from the valence to the conduction band through two virtual levels. However, if the photon energy is enough to cause a 2PA process, the absorption of two photons already promotes the electron from the valence band to a real level at the conduction band, and the third photon would be absorbed by a free carrier. Therefore, for the wavelengths where 2PA occurs, we expect that 2PA followed by FCA would be more probable than a simultaneous 2PA and 3PA process.

For a mechanism where FCA follows 2PA, the coefficient α_x can be related to the FCA cross-section σ and free-carrier density N by [24]

$$\alpha_x = \frac{\sigma N}{I^2} = \frac{\sigma \alpha_2 \sqrt{\pi} T I^2}{4\hbar\omega [1 - \exp(-t_p/\tau)]}, \quad (8)$$

where τ is the total free-carrier life-time, $t_p = 1/f_p$, and $T = \tau_{\text{FWHM}}/\sqrt{2\ln 2}$. Note that the third term of the right-hand side of Eq. (2), $\alpha_x I^3$, is equal to $\sigma N I$, as expected for a FCA process.

3. Results

Fig. 3 (a) presents typical plots of the output irradiance as a function of the input irradiance for the reference devices at 1490 nm. The intensities are calculated from the average power obtained experimentally using Eqs. (3) and (4). Fitting the data with Eq. (5), with $I(0)$, α_1 and $z = L$ as constants and α_2 as a fitting parameter, does not result in good agreement, suggesting another nonlinear absorption mechanism is present.

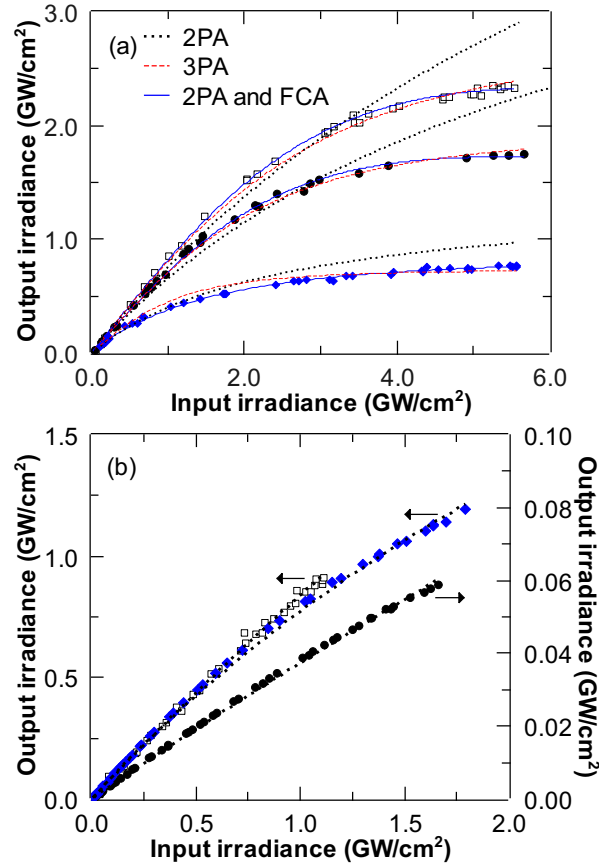


Fig. 3. (color on-line) Typical measurement results of the output irradiance as a function of the input irradiance and the corresponding nonlinear fit for the 2- μm -wide reference devices (a) and nanosectional parts (b), at a wavelength of 1490 nm. (\square) - strip-loaded, (\bullet) - nanowire, and (\blacklozenge) - half-core. Legend: 2PA - fitting with Eq. (5); 3PA - fitting with Eq. (6); 2PA and FCA - fitting with Eq. (7).

If 3PA alone is considered instead of 2PA, then Eq. (6) should be used for the fit. Fitting the experimental results with Eq. (6), with $I(0)$, α_1 , and $z = L$ as constants and α_3 as a fitting parameter, results in a better outcome than fitting them with Eq. (5). However, there are at least three indications against the interpretation of the nonlinear absorption as a 3PA mechanism. First, the 3PA coefficients α_3 achieved by the fitting are 0.39, 1.22, and 1.49 cm^3/GW^2 for the strip-loaded, half-core and nanowire geometries, respectively. These values are 10 to 40 times

greater than the value measured in Ref. [18] at 1500 nm. Second, from the 3PA scaling rule, it is expected that the 3PA coefficient increases with wavelength [18], but fitting the data at other wavelengths with Eq. (6) results in α_3 decreasing as λ increases. Third, the bandgap of the guiding layer material ($\text{Al}_{0.18}\text{Ga}_{0.82}\text{As}$) is about (1.66 ± 0.02) eV. This value was calculated by taking the mean and standard deviation of the bandgap energy reported in Refs. [13, 29–38]. From the bandgap value, the two-photon absorption edge is calculated as (1494 ± 18) nm, and the three-photon absorption edge as (2241 ± 27) nm. Therefore, at a wavelength of 1490 nm, a 3PA transition is not expected. The energy of two photons is enough to overcome the bandgap and promote a 2PA transition from the valence to the conduction band. The third photon of a hypothetical 3PA transition, in this case, is absorbed by an electron promoted to the conduction band, i.e., by a free carrier. The overall process then is 2PA followed by FCA, not a 3PA process. Thus, the fitted α_3 is an effective coefficient arising from the 2PA and FCA transitions instead of the actual 3PA process, which explains such a high α_3 value.

In this case, considering the mechanism of a 2PA transition followed by a free-carrier absorption would be more appropriate than extracting a 3PA coefficient. The 2PA-FCA analysis comprises fitting the data with Eq. (7). The fitting parameters are α_x and α_2 , while the constants are $z = L$, α_1 , and $I(0)$. The agreement between the fitting curve and experimental results in this case is even better than that obtained from fitting the results with Eq. (6). For the reference devices, the FCA cross-section, calculated by using the extracted fit parameter α_x and Eq. (8) are presented in Fig. 4 (a) while the α_2 results are presented in Fig. 5 (a). We discuss the α_2 results at the end of this section. Note that one could naively consider α_x as the 3PA coefficient (α_3) in an eventual simultaneous 2PA and 3PA effect. However, in this case, the same arguments against this interpretation given in the previous paragraph apply: α_3 results are one order of magnitude higher than what is presented in Ref. [18], α_3 decreases for longer wavelengths, and the bandgap value allows 2PA followed by FCA.

To calculate the FCA cross-section from α_x , we need to know the free-carrier lifetime [see Eq. (8)]. We assumed $\tau = 5$ ns, the same value as that used in Ref. [23] for a GaAs/AlGaAs waveguide, and the resulting σ is very close to what was reported in that reference. However, the lifetime found in the literature for GaAs/AlGaAs waveguides and quantum well structures, and AlGaAs waveguides, ranges from 0.06 ns to 35 ns [25, 39–42]. To evaluate what the FCA cross-section would be if a different τ was adopted, we used Eq. (8) and calculated σ for a wide range of lifetimes. The results are presented in Fig. 4 (b). We note that for $\tau \lesssim 35$ ns, the order of magnitude of σ would still be the same as presented in Fig. 4 (a): 10^{-16} cm².

The FCA cross-section of the strip-loaded and nanowire geometries slightly decreases when the wavelength increases. For the half-core device, σ is constant, given the error, but increases for longer wavelengths, which possibly indicates some residual effect of 3PA in this region.

For the tapered devices, calculating the nonlinear absorption coefficients is not as straightforward. The effective mode area changes along the propagation direction: it is the same as the reference devices for the coupling parts, and it is smaller for the nanosectional part. In order to evaluate the nonlinear absorption coefficient in the nanosectional part only, we performed the output vs. input power measurements as in the case of the reference devices, and then performed the analysis presented in Appendix B to calculate the input and output irradiance data points at the nanosectional part only, which are plotted in Fig. 3 (b). Here, Eq (5) fits the data well, indicating the absence of FCA effects. The linear and nonlinear losses cause the irradiance to drop along the coupling part such that the irradiance in the nanosectional part are sufficient to measure the 2PA coefficients, but too low to observe the effect of FCA. The corresponding α_2 values are presented in Fig. 5 (b).

Let us further discuss the results presented in Fig. 5. The 2PA coefficients for both the coupling and nanosectional parts decrease with increasing wavelength for all three geometries. We expect this behavior based on the 2PA scaling law, also considering that we are working

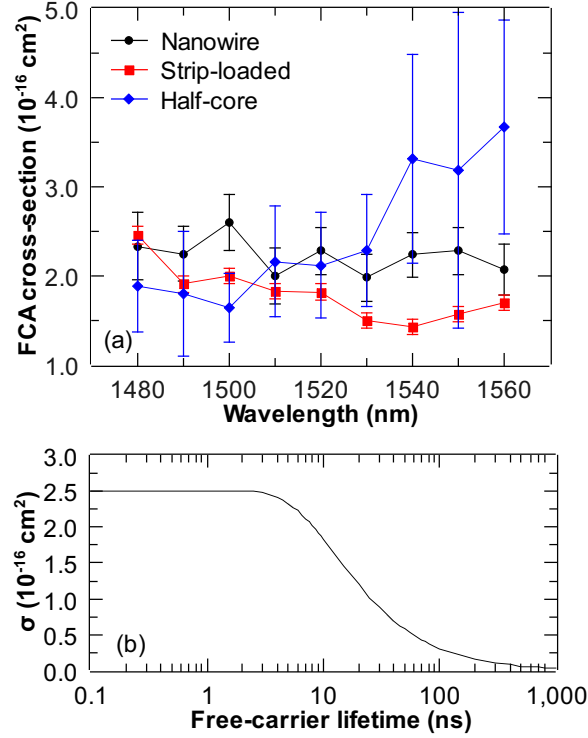


Fig. 4. (color on-line) (a) Free-carrier absorption cross-section as a function of wavelength for 2- μm -wide waveguides, assuming a free-carrier lifetime of 5 ns. (b) Free-carrier absorption cross-section calculated for different lifetimes for the 2- μm -wide nanowire waveguide.

near half-the-bandgap region [43]. However, α_2 does not drop to zero above half-the-bandgap [wavelengths longer than (1494 ± 18) nm] but continues to exponentially decrease, exhibiting a typical band tailing. Other works have reported an Urbach tail type of behavior for the two-photon absorption in AlGaAs, originating from defect states and impurities [12, 19, 20].

For the strip-loaded geometry with $\text{Al}_{0.18}\text{Ga}_{0.82}\text{As}$ guiding layer, the earlier reported values at the wavelength of 1500 nm (TE mode) are $\alpha_2 = (1.0 \pm 0.3)$, 0.8, and (1.15 ± 0.15) cm/GW, presented in Refs. [18], [19], and [20], respectively. These values agree well with our results for the nanosectional part of the strip-loaded geometry: (0.7 ± 0.3) cm/GW. The spectral behaviour is also very similar to that presented in Fig. 5 (b). There is no reported α_2 for waveguides of nanowire geometry whose guiding layer is made of $\text{Al}_{0.18}\text{Ga}_{0.82}\text{As}$, although Ref. [21] reports $\alpha_2 = 3.3$ cm/GW for a 1.5- μm -wide nanowire waveguide, with $\text{Al}_{0.13}\text{Ga}_{0.87}\text{As}$ the guiding layer, at 1550 nm. Moreover, the present work is the first to report on the 2PA coefficient measurement of the half-core waveguide geometry.

For both the reference or tapered devices, the value of α_2 is the highest for the half-core design, followed by the nanowire and then the strip-loaded. The difference between the results obtained for the three geometries is thought to be caused by the different nonlinear confinement factors or defects due to fabrication imperfection, as discussed further.

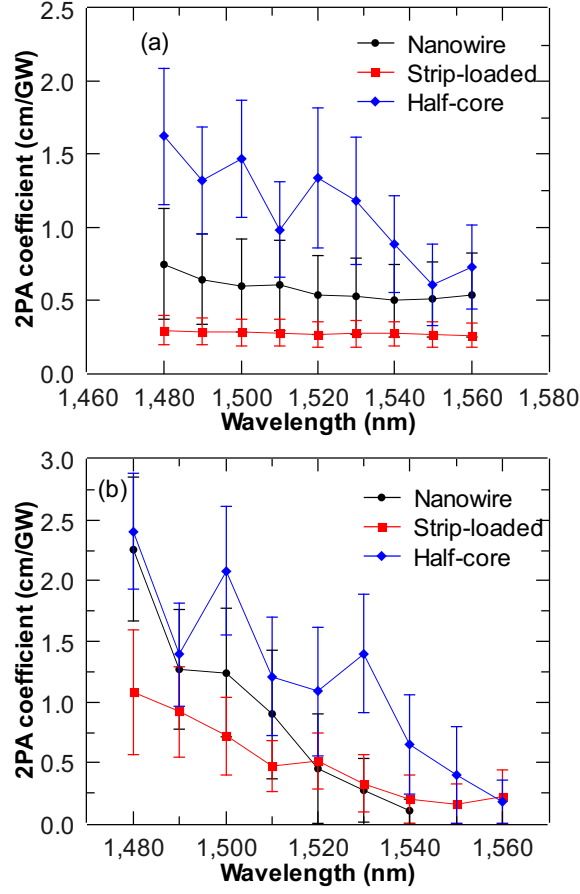


Fig. 5. (color on-line) The values of α_2 as a function of wavelength, experimentally measured for the 2- μm -wide waveguides (a) and the nanosectional parts (b).

4. Discussion

The modal field is not fully confined in the guiding layer region of the waveguides. It spreads into the claddings and the surrounding media in a geometry-dependent way [see the field distribution in Fig. 1 (c)-(h)]. Therefore, what is presented in Fig. 5 is the effective 2PA coefficient. Here, effective means the average value weighted by the irradiance of each material.

In Ref. [44], the authors proposed the formula to calculate the effective nonlinear refractive index and indicated how to adapt their approach to calculate the effective 2PA coefficient ($\alpha_{2,\text{eff}}$). Based on their suggestion, we derived

$$\alpha_{2,\text{eff}} = \Gamma_{2,(1)}\alpha_{2,(1)} + \Gamma_{2,(2)}\alpha_{2,(2)} + \dots, \quad (9)$$

where $\Gamma_{2,M}$ ($\alpha_{2,M}$) is the third-order nonlinear confinement factor (2PA coefficient) for each material (or each layer), M , of the waveguide structure. The nonlinear confinement factor is calculated by

$$\Gamma_{2,M} = \frac{\int_M I^2(x, y) dA}{\int_{-\infty}^{\infty} I^2(x, y) dA}. \quad (10)$$

The integral in the numerator of Eq. (10) is performed only over the area of the material M (either the guiding layer or the cladding), and $I(x, y)$ denotes the irradiance at the position (x, y) of the transverse mode [44]. The bandgap energy of the cladding materials, $\text{Al}_{0.35}\text{Ga}_{0.65}\text{As}$ and $\text{Al}_{0.65}\text{Ga}_{0.35}\text{As}$ [see fig. 1 (c)-(h) for the material composition of each layer], are about 1.93 and 2.40 eV, respectively [13]. For this reason, the 2PA coefficients of the cladding materials are expected to be very small for wavelengths longer than 1288 nm and 1033 nm for cladding layer compositions of $\text{Al}_{0.35}\text{Ga}_{0.65}\text{As}$ and $\text{Al}_{0.65}\text{Ga}_{0.35}\text{As}$ respectively, and negligible in the wavelength range of this work. Hence, we expect that the effective 2PA coefficient in each geometry is related to the nonlinear confinement factor of the guiding layer ($\Gamma_{2,\text{guid}}$) by the equation

$$\alpha_{2,\text{eff}} = \Gamma_{2,\text{guid}}\alpha_{2,\text{guid}}. \quad (11)$$

To interpret the results presented in Fig. 5, let us first suppose that the guiding layer of the three geometries is made solely from $\text{Al}_{0.18}\text{Ga}_{0.82}\text{As}$. Let us also assume that the defects and impurities concentration in the guiding layer are the same for the three geometries. Then the material $\alpha_{2,\text{guid}}$ should be the same for the three geometries. Based on Eq. (11), the effective 2PA coefficient should be different for each geometry or each waveguide part if the nonlinear confinement factors are not the same. Fig. 6 presents the effective 2PA coefficient as a function of the nonlinear confinement factor of the waveguide's guiding layer for the three geometries at the nanosectional part and for the reference device. $\Gamma_{2,\text{guid}}$ was calculated with FDE solver of *Lumerical Mode Solutions*, using the *integrate* function to implement Eq. (10). The effective 2PA coefficient slowly increases with the increase of the nonlinear confinement factor. By fitting the data with Eq. (11), we found $\alpha_{2,\text{guid}} = 1.1 \text{ cm/GW}$. However, some points do not agree with the fitted curve, which is an indication that other factors, besides $\Gamma_{2,\text{guid}}$, influence our α_2 results.

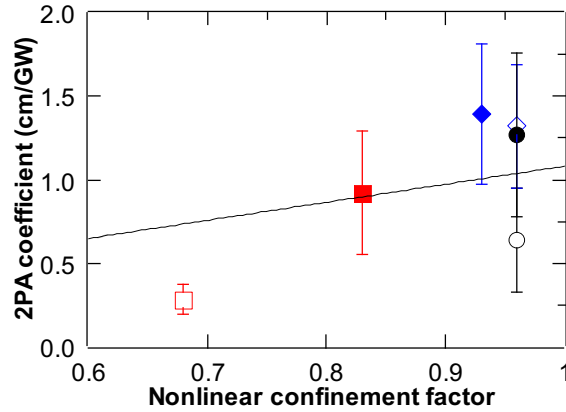


Fig. 6. (color on-line) Effective α_2 at 1490 nm as a function of the waveguide's guiding layer nonlinear confinement factor $\Gamma_{2,\text{guid}}$. 2- μm -wide waveguides: (□) - strip-loaded, (○) - nanowire, and (◇) - half-core. Nanosectional parts: (■) - strip-loaded, (●) - nanowire, and (◆) - half-core. The solid line is a fitting with Eq. (11), resulting in $\alpha_{2,\text{guid}} = 1.1 \text{ cm/GW}$.

Fabrication imperfections might have affected our results in two ways. First, the sidewall roughness of the waveguide's guiding layer can be present in the nanowire and half-core geometry because the guiding layer (or part of it) is etched through [Fig. 1 (g) and (h)]. The strip-loaded geometry, on the other hand, is less susceptible to such roughness because the guiding layer is fully covered by the upper cladding [Fig. 1 (f)]. Hence, nonlinear scattering or defect states might have contributed to the higher values of the 2PA coefficient for the nanowire and half-core

geometries. Second, we used the characteristics of the reference waveguides [Fig. 1 (b)] to evaluate the linear and nonlinear absorption contributions of the coupling parts of the device [see Fig. 1 (a)]. However, since the reference waveguide is a separate device, its characteristics might slightly differ from those of the coupling parts, thereby affecting the precision of determining the nanosectional part's 2PA coefficient.

Based on our results, we highlight two important considerations for the evaluation of nonlinear absorption in waveguides. First, the effective 2PA coefficient is geometry-dependent and may be affected by fabrication imperfections. For this reason, the measurement of 2PA coefficient in the actual fabricated device, rather than taking the α_2 value from the literature for similar material composition, is preferable. Second, Eqs. (9) and (10) can be used to evaluate the effective 2PA for specific compositions and geometries when designing the waveguides. The aluminum fraction x is often used as a design parameter to determine the 2PA edge wavelength and how strong 2PA would be at a particular wavelength range [12]. Our work suggests that $\Gamma_{2,\text{guid}}$ can also be used as a design parameter to evaluate the geometry-dependent 2PA.

5. Conclusion

We demonstrated that the two-photon absorption coefficients of AlGaAs waveguides of three different geometries with the same compositions of the guiding layers have different values. We pointed out two factors contributing to this discrepancy. First, the confinement of the electric field at the waveguide's guiding region is geometry-dependent and varies for different widths of same kind of devices. As the three AlGaAs layers comprising the waveguides have different aluminum fractions, the measured effective 2PA coefficient depends on whether the irradiance is more or less confined in one or another layer. We used the third-order nonlinear confinement factor to evaluate this effect. Second, fabrication imperfections in each geometry also contribute to the differences in the effective 2PA coefficient values. On average, the half-core geometry presented higher 2PA coefficients, followed by the nanowire and then the strip-loaded waveguide. Therefore, measuring the 2PA coefficient for a new waveguide geometry and/or material composition is better than taking the corresponding values from the literature. Furthermore, the free-carrier absorption cross-sections determined by our method do not present a clear geometry dependence.

Appendix A: Linear loss

The linear loss coefficients of the reference devices and the nanosectional parts are presented in Fig. 7 (a) and (b), respectively. For the strip-loaded and nanowire waveguides, the linear loss is almost constant across the whole wavelength range. Yet, it is higher in the nanowires than in the strip-loaded waveguides. This is thought to be caused by the sidewall roughness of the exposed sidewalls of the nanowire guiding layer, leading to higher scattering losses in the nanowires [3]. Since the mode in the nanowire is confined in the region that is etched through, the sidewall surface exposed to air tends to have surface roughness. In addition, any oxidation on the sidewall's surface can impact the mode's propagation. In contrast, the guiding layer region in the strip-loaded waveguides is buried underneath the upper cladding. The interfaces between AlGaAs layers tend to be smoother than the etched sidewalls, leading to fewer scattering centers. We expect the linear loss coefficient of the half-core geometry to be in between that of the strip-loaded and nanowire since only a part of the guiding layer region is exposed to the air with sidewall roughness. This trend is observed for the narrowest parts of the waveguides [Fig. 7 (b)]. However, for the reference devices, the half-core has the highest linear loss, which fluctuates from wavelength to wavelength [Fig. 7 (a)], possibly because of a higher scattering at the waveguide's input and output facets [1]. As a result, the uncertainty in determining the 2PA coefficient and FCA cross-section is higher for the half-core geometry.

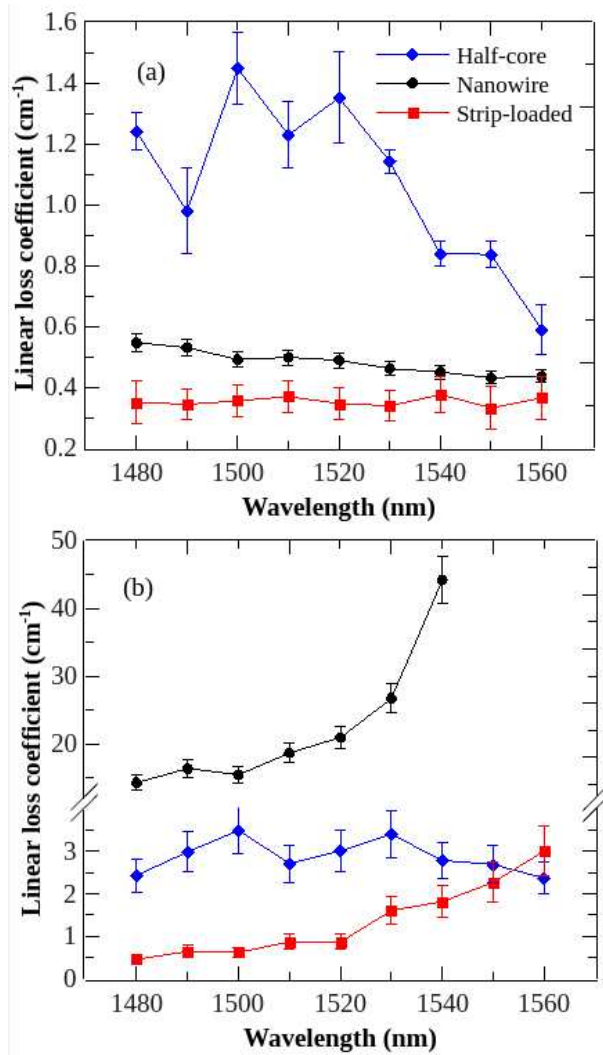


Fig. 7. (color on-line) Linear loss coefficient α_1 as a function of wavelength for the 2- μm -wide waveguides (a) and for the nanosectional parts (b).

Appendix B: Calculation of the irradiance in the waveguide's nanosectional part

The input (P_{in}) and output (P_{out}) power were measured for the tapered devices by using the nonlinear transmittance technique [see Fig. 1 (a) to locate the z positions presented in this analysis]. The irradiance at the input [$I(0)$] and output [$I(L)$] of the device were calculated with Eq. (3) and (4), respectively, by using the P_{in} and P_{out} experimental data.

The following method was used to calculate the irradiance data points at the beginning and end of the nanosectional part, as presented in Fig. 3 (b).

1. We suppose that a 2PA process followed by FCA also occurs at the input coupler (the first part of the waveguide with length L_C). Then, the irradiance at the end of the input coupling part [$I(L_C)$] is calculated by Eq. (7). The other parameters used in this calculation, besides $z = L_C$ and $I(0)$, are α_1 , α_2 and α_x of the reference devices.

2. The x -coordinate of the data points in Fig. 3 (b) is the irradiance at the input of the nanosectional part. It was calculated by $I(L + L_C + L_t) = I(L_C)(t_1 A_{\text{eff}}^C / A_{\text{eff}}^{\text{NS}})$, where A_{eff}^C and $A_{\text{eff}}^{\text{NS}}$ are the effective area of the coupling and nanosectional parts, respectively, and t_1 is the taper loss coefficient of each taper.
3. Similarly, the y -coordinate of the data points in Fig. 3 (b) is the irradiance at the output of the nanosectional part. It was calculated by $I(L + L_C + L_t + L_{\text{NS}}) = I(L - L_C)A_{\text{eff}}^C / (t_1 A_{\text{eff}}^{\text{NS}})$.
4. To calculate $I(L - L_C)$, we suppose that there is only linear loss at the output coupler, so $I(L - L_C) = I(L)e^{\alpha_1 L_C}$, with α_1 of the reference devices, and $I(L)$ given by Eq. (4).

The linear loss in the taper parts is given by the taper loss coefficient (t_1), which is the fraction of power transmitted through each 0.2-mm-long taper. It was determined as $t_1 = 0.89$ for the nanowire and $t_1 = 1$ for the strip-loaded and half-core geometries, by comparing the transmission of reference and taper-to-taper ($L_{\text{NS}} = 0$) devices. Due to the short taper length in comparison to L_C or L_{NS} , the nonlinear losses in the tapers were neglected.

Funding. The financial support was provided by Canada First Research Excellence Fund award on Transformative Quantum Technologies, the Natural Sciences and Engineering Council of Canada (Discovery and RTI programs) and the Canada Research Chairs program. The epitaxial growth of AlGaAs wafers was supported by a CMC Microsystems award.

Disclosures. The authors declare no conflicts of interest

Data availability. Data underlying the results presented in this paper are not publicly available at this time but may be obtained from the authors upon reasonable request.

References

1. D. H. G. Espinosa, K. M. Awan, M. Odungide, S. R. Harrigan, D. R. Sanchez, and K. Dolgaleva, "Tunable four-wave mixing in AlGaAs waveguides of three different geometries," *Opt. Commun.* **479**, 126450 (2021).
2. M. Pu, H. Hu, L. Ottaviano, E. Semenova, D. Vukovic, L. K. Oxenløwe, and K. Yvind, "Ultra-efficient and broadband nonlinear AlGaAs-on-insulator chip for low-power optical signal processing," *Laser Photonics Rev.* **12**, 1800111 (2018).
3. K. Dolgaleva, P. Sarrafi, P. Kultavewuti, K. M. Awan, N. Feher, J. S. Aitchison, L. Qian, M. Volatier, R. Arès, V. Aimez, and et al., "Tuneable four-wave mixing in AlGaAs nanowires," *Opt. Express* **23**, 22477 (2015).
4. K. A. Johnson and J. S. Aitchison, "Orthogonal four wave mixing in AlGaAs nanowire waveguides," in *CLEO: QELS Fundamental Science*, (Optical Society of America, 2019), pp. JW2A-36.
5. P. M. Kaminski, F. Da Ros, E. P. da Silva, M. Pu, M. P. Yankov, E. Semenova, K. Yvind, A. T. Clausen, S. Forchhammer, L. K. Oxenløwe *et al.*, "Characterization and optimization of four-wave-mixing wavelength conversion system," *J. Light. Technol.* **37**, 5628-5636 (2019).
6. F. Da Ros, M. P. Yankov, E. P. da Silva, M. Pu, L. Ottaviano, H. Hu, E. Semenova, S. Forchhammer, D. Zibar, M. Galili *et al.*, "Characterization and optimization of a high-efficiency AlGaAs-on-insulator-based wavelength converter for 64-and 256-QAM signals," *J. Light. Technol.* **35**, 3750-3757 (2017).
7. H. Hu, F. Da Ros, M. Pu, F. Ye, K. Ingerslev, E. P. da Silva, M. Nooruzzaman, Y. Amma, Y. Sasaki, T. Mizuno *et al.*, "Single-source chip-based frequency comb enabling extreme parallel data transmission," *Nat. Photonics* **12**, 469-473 (2018).
8. M. Savanier, A. Andronico, A. Lemaître, C. Manquest, I. Favero, S. Ducci, and G. Leo, "Nearly-degenerate three-wave mixing at 1.55 μm in oxidized algaas waveguides," *Opt. express* **19**, 22582-22587 (2011).
9. S. May, M. Kues, M. Clerici, and M. Sorel, "Second-harmonic generation in AlGaAs-on-insulator waveguides," *Opt. letters* **44**, 1339-1342 (2019).
10. D. Duchesne, K. Rutkowska, M. Volatier, F. Légaré, S. Delprat, M. Chaker, D. Modotto, A. Locatelli, C. De Angelis, M. Sorel *et al.*, "Second harmonic generation in AlGaAs photonic wires using low power continuous wave light," *Opt. express* **19**, 12408-12417 (2011).
11. S. Gehrsitz, F. K. Reinhart, C. Gourgon, N. Herres, A. Vonlanthen, and H. Sigg, "The refractive index of $\text{Al}_x\text{Ga}_{1-x}\text{As}$ below the band gap: accurate determination and empirical modeling," *J. Appl. Phys.* **87**, 7825-7837 (2000).
12. G. I. Stegeman, A. Villeneuve, J. Kang, J. S. Aitchison, C. N. Ironside, K. Al-Hemyari, C. C. Yang, C.-H. Lin, H.-H. Lin, G. T. Kennedy, R. S. Grant, and S. W., "AlGaAs below half bandgap: the silicon of nonlinear optical materials," *Int. J. Nonlinear Opt. Phys.* **3**, 347-371 (1994).
13. C. Bosio, J. L. Staehli, M. Guzzi, G. Burri, and R. A. Logan, "Direct-energy-gap dependence on Al concentration in $\text{Al}_x\text{Ga}_{1-x}\text{As}$," *Phys. Rev. B* **38**, 3263 (1988).

14. S. Adachi, "Optical properties of $\text{Al}_x\text{Ga}_{1-x}\text{As}$ alloys," *Phys. Rev. B* **38**, 12345 (1988).
15. E. W. Van Stryland, Y.-Y. Wu, D. J. Hagan, M. Soileau, and K. Mansour, "Optical limiting with semiconductors," *JOSA B* **5**, 1980–1988 (1988).
16. K. Nozaki, T. Tanabe, A. Shinya, S. Matsuo, T. Sato, H. Taniyama, and M. Notomi, "Sub-femtojoule all-optical switching using a photonic-crystal nanocavity," *Nat. Photonics* **4**, 477–483 (2010).
17. V. Van, T. Ibrahim, K. Ritter, P. Absil, F. Johnson, R. Grover, J. Goldhar, and P.-T. Ho, "All-optical nonlinear switching in GaAs-AlGaAs microring resonators," *IEEE Photonics Technol. Lett.* **14**, 74–76 (2002).
18. J. Aitchison, D. Hutchings, J. Kang, G. Stegeman, and A. Villeneuve, "The nonlinear optical properties of AlGaAs at the half band gap," *IEEE J. Quantum Electron.* **33**, 341–348 (1997).
19. J. U. Kang, A. Villeneuve, M. Sheik-Bahae, G. I. Stegeman, K. Al-hemyari, J. S. Aitchison, and C. N. Ironside, "Limitation due to three-photon absorption on the useful spectral range for nonlinear optics in AlGaAs below half band gap," *Appl. Phys. Lett.* **65**, 147–149 (1994).
20. A. Villeneuve, C. C. Yang, G. I. Stegeman, C. Lin, and H. Lin, "Nonlinear refractive-index and two photon-absorption near half the band gap in AlGaAs," *Appl. Phys. Lett.* **62**, 2465–2467 (1993).
21. J. J. Wathen, P. Apiratikul, C. J. Richardson, G. A. Porkolab, G. M. Carter, and T. E. Murphy, "Efficient continuous-wave four-wave mixing in bandgap-engineered AlGaAs waveguides," *Opt. letters* **39**, 3161–3164 (2014).
22. K. M. Awan, N. Feher, R. Boyd, and K. Dolgaleva, "Aluminium gallium arsenide waveguide designs for efficient four-wave mixing," in *2015 Photonics North*, (IEEE, 2015), pp. 1–1.
23. A. Villeneuve, C. C. Yang, G. I. Stegeman, C. N. Ironside, G. Scelsi, and R. M. Osgood, "Nonlinear absorption in a GaAs waveguide just above half the band gap," *IEEE journal quantum electronics* **30**, 1172–1175 (1994).
24. F. R. Laughton, J. H. Marsh, and J. S. Roberts, "Intuitive model to include the effect of free-carrier absorption in calculating the two-photon absorption coefficient," *Appl. physics letters* **60**, 166–168 (1992).
25. F. Laughton, J. Marsh, and C. Button, "Time-resolved nonlinear absorption modulation in GaAs/AlGaAs multiple-quantum-well waveguides at $1.06\ \mu\text{m}$," *IEEE photonics technology letters* **4**, 863–866 (1992).
26. K. Awan, "Fabrication of III-V integrated photonic devices," Ph.D. thesis, University of Ottawa (2018).
27. G. Tittelbach, B. Richter, and W. Karthe, "Comparison of three transmission methods for integrated optical waveguide propagation loss measurement," *Pure Appl. Opt. J. Eur. Opt. Soc. Part A* **2**, 683 (1993).
28. G. Boudebs, S. Cherukulappurath, M. Guignard, J. Troles, F. Smektala, and F. Sanchez, "Experimental observation of higher order nonlinear absorption in tellurium based chalcogenide glasses," *Opt. Commun.* **232**, 417–423 (2004).
29. M. El Allali, C. B. Sørensen, E. Veje, and P. Tidemand-Petersson, "Experimental determination of the GaAs and $\text{Ga}_{1-x}\text{Al}_x\text{As}$ band-gap energy dependence on temperature and aluminum mole fraction in the direct band-gap region," *Phys. Rev. B* **48**, 4398 (1993).
30. D. Huang, G. Ji, U. K. Reddy, H. Morkoç, F. Xiong, and T. A. Tombrello, "Photorefectance, absorption, and nuclear resonance reaction studies of $\text{Al}_x\text{Ga}_{1-x}\text{As}$ grown by molecular-beam epitaxy," *J. Appl. Phys.* **63**, 5447–5453 (1988).
31. J. M. Wrobel, L. C. Bassett, J. L. Aubel, S. Sundaram, J. L. Davis, and J. Comas, "Variations of energies and line shapes of the electroreflectance spectra of epitaxial $\text{Al}_x\text{Ga}_{1-x}\text{As}$," *J. Vac. Sci. & Technol. A: Vacuum, Surfaces, Films* **5**, 1464–1469 (1987).
32. G. Oelgart, R. Schwabe, M. Heider, and B. Jacobs, "Photoluminescence of $\text{Al}_x\text{Ga}_{1-x}\text{As}$ near the γ -x crossover," *Semicond. science technology* **2**, 468 (1987).
33. D. E. Aspnes, S. M. Kelso, R. A. Logan, and R. Bhat, "Optical properties of $\text{Al}_x\text{Ga}_{1-x}\text{As}$," *J. applied physics* **60**, 754–767 (1986).
34. J. L. Aubel, U. K. Reddy, S. Sundaram, W. T. Beard, and J. Comas, "Interband transitions in molecular-beam-epitaxial $\text{Al}_x\text{Ga}_{1-x}\text{As}/\text{GaAs}$," *J. Appl. Phys.* **58**, 495–498 (1985).
35. N. C. Miller, S. Zemon, G. P. Werber, and W. Powazinik, "Accurate electron probe determination of aluminum composition in (Al, Ga)As and correlation with the photoluminescence peak," *J. Appl. Phys.* **57**, 512–515 (1985).
36. H. J. Lee, L. Y. Juravel, J. C. Woolley, and A. J. SpringThorpe, "Electron transport and band structure of $\text{Ga}_{1-x}\text{Al}_x\text{As}$ alloys," *Phys. Rev. B* **21**, 659 (1980).
37. H. C. Casey Jr, "Room-temperature threshold-current dependence of GaAs- $\text{Al}_x\text{Ga}_{1-x}\text{As}$ double-heterostructure lasers on x and active-layer thickness," *J. Appl. Phys.* **49**, 3684–3692 (1978).
38. B. Monemar, K. K. Shih, and G. D. Pettit, "Some optical properties of the $\text{Al}_x\text{Ga}_{1-x}\text{As}$ alloys system," *J. Appl. Phys.* **47**, 2604–2613 (1976).
39. D. Szymanski, B. Jones, M. Skolnick, A. Fox, D. O'Brien, T. Krauss, and J. Roberts, "Ultrafast all-optical switching in AlGaAs photonic crystal waveguide interferometers," *Appl. Phys. Lett.* **95**, 141108 (2009).
40. J. Ma, J. Chiles, Y. D. Sharma, S. Krishna, and S. Fathpour, "Two-photon photovoltaic effect in gallium arsenide," *Opt. letters* **39**, 5297–5300 (2014).
41. P. Apiratikul, "Semiconductor waveguides for nonlinear optical signal processing," Ph.D. thesis (2009).
42. J. Orton, P. Dawson, D. Lacklison, T. Cheng, and C. Foxon, "Recombination lifetime measurements in AlGaAs/GaAs quantum well structures," *Semicond. science technology* **9**, 1616 (1994).
43. B. S. Wherrett, "Scaling rules for multiphoton interband absorption in semiconductors," *J. Opt. Soc. Am. B* **1**, 67–72 (1984).
44. R. Grant, "Effective non-linear coefficients of optical waveguides," *Opt. Quantum Electron.* **28**, 1161–1173 (1996).